

Wigner tomography of multispin quantum states

David Leiner,^{1,*} Robert Zeier,^{1,†} and Steffen J. Glaser^{1,‡}

¹*Technische Universität München, Department Chemie, Lichtenbergstrasse 4, 85747 Garching, Germany*

(Dated: January 15, 2018)

We study the tomography of multispin quantum states in the context of finite-dimensional Wigner representations. An arbitrary operator can be completely characterized and visualized using multiple shapes assembled from linear combinations of spherical harmonics [A. Garon, R. Zeier, and S. J. Glaser, Phys. Rev. A 91, 042122 (2015)]. We develop a general methodology to experimentally recover these shapes by measuring expectation values of rotated axial spherical tensor operators and provide an interpretation in terms of fictitious multipole potentials. Our approach is experimentally demonstrated for quantum systems consisting of up to three spins using nuclear magnetic resonance spectroscopy.

Keywords: Nuclear magnetic resonance, Quantum tomography, Phase space methods

I. INTRODUCTION

Optical homodyne tomography can be applied to experimentally measure the quantum state of light [1–5]. One thereby recovers an infinite-dimensional Wigner function [6–8] as a classically motivated phase-space representation, providing a useful tool for the characterization and visualization of quantum-optical systems [9]. This results in an advantageous dualism between measurement scheme and phase-space representation, which we would like to transfer to the case of finite-dimensional, *coupled* spin systems.

One important representation of finite-dimensional quantum systems relies on discrete Wigner functions [10–15]. But we will restrict ourselves to continuous representations in order to naturally reflect the inherent rotational symmetries of spins. Individual spins are faithfully described by their magnetization vector (or Bloch vector), which, however, neglects relevant parts of the full density matrix in the case of multiple, coupled spins. These missing parts include zero- and multiple-quantum or antiphase coherence as well as spin alignment [16], which are partially characterized by visual approaches based on single-transition operators [16–18].

We will follow the general strategy of Stratonovich [19] which specifies criteria for the definition of continuous Wigner functions for finite-dimensional quantum systems. The case of single spins is widely studied in the literature [20–25], and visualizations for multiple spins have been considered in [7, 26–29] with various degrees of generality. However, until very recently, it was not clear [28, 29] if a general Wigner representation also exists for arbitrary, coupled spin systems, and even the case of three coupled spins $1/2$ was open.

Fortunately, a general Wigner representation for characterizing and visualizing arbitrary coupled spin systems

has been developed in [30]. It is based on mapping arbitrary operators to a set of spherical functions which are denoted as droplets, while preserving crucial features of the quantum system. The characteristic shapes of these droplets can be interpreted as the result of an abstract mapping, but we also ask in this paper how they are related to experimentally measurable quantities. The general Wigner representation introduced in [30] is denoted as the DROPS representation (discrete representation of operators for spin systems), and its basics are recalled in Sec. II where important properties are also summarized.

In this paper, we theoretically develop a tomography scheme for spherical functions of arbitrary multispin quantum states. We study experimental schemes to reconstruct the generalized Wigner representation of a given density operator (representing mixed or pure quantum states). Extensions to quantum process tomography [31] as given by the experimental reconstruction of entire propagators (e.g., representing quantum gates) are, however, beyond the scope of this paper. Our scheme is particularly tailored to the Wigner representation of [30], for which an interpretation in terms of fictitious multipole potentials is provided. We will focus on systems consisting of spins $1/2$, even though our approach is applicable to arbitrary spin numbers. We also provide explicit experimental protocols for our Wigner tomography scheme and demonstrate its feasibility using nuclear magnetic resonance (NMR) experiments. Motivated by our experiments, most of the discussed examples consider only the traceless part of the density matrix.

This paper is organized as follows. A brief summary of the DROPS representation is presented in Sec. II. Our general methodology for sampling spherical functions of multispin operators is introduced in Sec. III, which also states the main technical results for the Wigner tomography. Section IV provides a physical interpretation of spherical functions in terms of fictitious multipole potentials. The performed NMR experiments are summarized in Sec. V, and Sec. VI discusses the use of temporal averaging. The precise experimental scheme and its implementation on a spectrometer are detailed in Secs. VII and VIII. We conclude by summarizing and discussing theo-

* david.leiner@tum.de

† zeier@tum.de

‡ steffen.glaser@tum.de

retical and experimental aspects, while also contrasting our paper with other tomography approaches. Further details are deferred to the Appendices.

II. VISUALIZATION OF OPERATORS USING SPHERICAL FUNCTIONS

We summarize the approach of [30] to obtain a Wigner representation of arbitrary operators A in coupled spin systems using multiple spherical functions, which is based on a general one-to-one mapping from spherical tensor operators to spherical harmonics. An operator

$$A = \sum_{\ell \in L} A^{(\ell)} \quad (1)$$

is decomposed according to a suitable set L of labels ℓ (i.e. quantum numbers) inducing a bijective mapping between the components $A^{(\ell)}$ and spherical functions $f^{(\ell)} = f^{(\ell)}(\theta, \phi)$. These spherical functions can be plotted together as seen in the example of Fig. 1(a) where the corresponding mapping is highlighted. This provides a pictorial representation of the operator A , which conserves important properties and symmetries depending on the chosen label set L .

The components $A^{(\ell)}$ and the spherical functions $f^{(\ell)} = f^{(\ell)}(\theta, \phi)$ can be further split up into their multipole contributions $A_j^{(\ell)}$ and $f_j^{(\ell)} = f_j^{(\ell)}(\theta, \phi)$ depending on the ranks $j \in J(\ell)$ occurring for each label ℓ as shown in Fig. 1(b), i.e.,

$$A^{(\ell)} = \sum_{j \in J(\ell)} A_j^{(\ell)} \quad \text{and} \quad f^{(\ell)} = \sum_{j \in J(\ell)} f_j^{(\ell)}. \quad (2)$$

Finally, the rank- j multipole contributions [see Fig. 1(c)]

$$A_j^{(\ell)} = \sum_{m=-j}^j c_{jm}^{(\ell)} T_{jm}^{(\ell)} \quad \text{and} \quad f_j^{(\ell)} = \sum_{m=-j}^j c_{jm}^{(\ell)} Y_{jm}, \quad (3)$$

can be decomposed into components of irreducible spherical tensor operators $T_{jm}^{(\ell)}$ [32–37] and the corresponding spherical harmonics Y_{jm} [38, 39] of order m with $-j \leq m \leq j$. Note the identical expansion coefficients $c_{jm}^{(\ell)}$ in Eq. (3). The dualism in Eqs. (2) and (3) exploits the well-known correspondence between irreducible tensor operators and spherical harmonics [36, 37]. In summary, an operator A is mapped to a set of spherical functions $f^{(\ell)}$, each of which is referred to as a droplet identified by ℓ . The whole representation (and its visualization) was introduced in [30] and is denoted as the DROPS representation (discrete representation of operators for spin systems), and it lends itself to interactively exploring the dynamics of multispin systems, e.g., by use of the free application [40].

The example presented in Fig. 1 uses one particular version of this representation which relies on the LISA

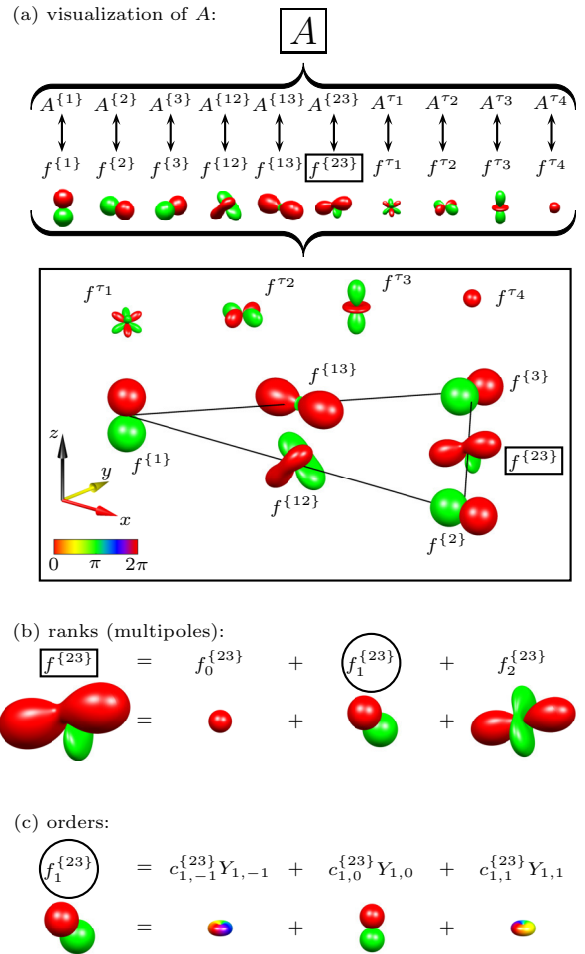


FIG. 1. (Color online) (a) Three-spin operator $A = I_{1z} + I_{2x} + I_{3y} + 2I_{1x}I_{2z} + I_{2x}I_{3x} + I_{2x}I_{3y} + I_{2x}I_{3z} + 2I_{1x}I_{3x} + 4I_{1x}I_{2x}I_{3x}$ [16, 41] visualized using multiple spherical functions $f^{(\ell)} = f^{(\ell)}(\theta, \phi)$, and individual components $A^{(\ell)}$ of A mapped to $f^{(\ell)}$ and graphically visualized; A^0 is here zero; trilinear labels $\{\{123\}, \tau_p\}$ are shortened to $\{\tau_p\}$. (b) $f^{\{23\}}$ (box) decomposed into its 2^j -multipole contributions $f_j^{\{23\}}$ with $j \in \{0, 1, 2\}$ (monopole, dipole, and quadrupole) (c) $f_1^{\{23\}}$ (circle) decomposed into spherical harmonics of order $m \in \{-1, 0, 1\}$; $Y_{1,-1}$ and $Y_{1,1}$ are rainbow colored [42].

tensor operator basis as defined in [30], which is characterized by the linearity of the basis operators, the involved subsystem, and auxiliary criteria, such as permutation symmetry. For coupled spins 1/2, operators are first decomposed in this basis according to the set of involved spins, e.g., one introduces the labels $\{k\}$ and $\{kl\}$ for linear and bilinear operators acting on a subset of one or two spins numbered by k and l , and so forth. Secondly, the LISA basis for operators acting on three or more spins needs to also distinguish symmetry properties under permutations, i.e., combined labels such as $\{\{klm\}, \tau_p\}$ are used, where the permutation symmetry type τ_p is given by a Young tableau [43]. Finally, further *ad hoc* labels are necessary for operators involving six or more spins. Arbi-

bitrary operators of a coupled spin system can be uniquely represented using this LISA tensor operator basis. Additional details for the visualization technique are given in [30] which also discusses alternative labeling approaches for DROPS representations.

The presented Wigner representation can be applied to general mixed quantum states as represented by the density operator, and it is not limited to pure quantum states as given by a state function. In fact, it can be used to represent arbitrary operators of spin systems: examples include Hermitian operators as Hamiltonians or density operators representing observables as well as non-Hermitian operators such as propagators or general quantum gates [30].

The Wigner representation using the LISA basis is particularly attractive for the visualization and analysis of quantum states in magnetic resonance spectroscopy [16] and quantum information processing [44] and its properties have been discussed in [30].

(a) The *location* of the droplets informs about which and how many spin operators are involved in a given quantum state and what symmetries under particle exchange are present [c.f. Fig. 1(a)].

(b) The *shape* and *colors* of the droplets reflect spectroscopically important properties. For example, states with defined coherence order p [16] can be recognized by their axially symmetric shape, and the magnitude as well as sign of the coherence order p are represented by the number and direction of “rainbows” per revolution around the z axis [see Figs. 5 and 6]. This also allows us to recognize characteristic states, such as inphase and anti-phase coherences.

(c) Furthermore, our representation directly depicts information about reduced density matrices and thereby conveys information related to entanglement measures, which would have to be first computed from the density-matrix description via partial traces. In particular, the size of the droplets corresponding to linear terms [positioned in the vertices of the triangle in Fig. 1(a)] provides information on the amount of bipartite entanglement measured by the concurrence (see Sec. IV E in [30]). This is an example of the fact that relevant information is often determined already by a subset of all droplets in the LISA basis. The LISA basis thereby offers a more structured picture than the density matrix, even though the number of droplets grows rapidly with increasing number of spins. However, as pointed out in [30], this number grows less rapidly than the number of density matrix elements.

(d) The droplets *rotate* under non-selective pulses in a natural way. In combination with the characteristic droplet shapes, this property makes it in many cases possible to design experiments that transfer a given initial state into a desired target state without detailed calculations. Beyond merely interpreting the occurring characteristic shapes as a result of an abstract mapping, it is interesting to ask whether they are connected to experimentally measurable quantities.

III. SAMPLING SPHERICAL FUNCTIONS OF MULTI-SPIN OPERATORS

We explain now how the shape of spherical functions can be characterized by suitable chosen spherical samples. This will be particularly relevant for spherical functions representing spin operators as discussed in Sec. II for which these spherical samples can be experimentally measured. One obtains a reconstruction method for the quantum state in terms of spherical functions. In the general case, the associated rank- j components $g_j(\theta, \phi)$ of an arbitrary spherical function $g(\theta, \phi)$ are determined by its scalar product with rotated versions $R_{\alpha\beta}Y_{j0}(\theta, \phi)$ of axial spherical harmonics $Y_{j0}(\theta, \phi)$, which have rank j and order zero. Given two spherical functions $h(\theta, \phi)$ and $g(\theta, \phi)$, we recall the definition of their scalar product $\langle h(\theta, \phi) | g(\theta, \phi) \rangle_{L^2} := \int_{\theta=0}^{\pi} \int_{\phi=0}^{2\pi} h^*(\theta, \phi) g(\theta, \phi) \sin\theta d\theta d\phi$. The rotation operator $R_{\alpha\beta}$ acts on a spherical function $h(\theta, \phi)$ by first rotating it around the y axis by a polar angle β and then rotating the result around the z axis by an azimuthal angle α , i.e., $R_{\alpha\beta}h(\theta, \phi) := h[R_{\alpha\beta}^{-1}(\theta, \phi)] = h(\theta - \beta, \phi - \alpha)$. After these preparations, the mathematical result underpinning our reconstruction method states that the value of the rank- j component $g_j(\beta, \alpha)$ is proportional to the scalar product of $R_{\alpha\beta}Y_{j0}(\theta, \phi)$ with $g(\theta, \phi)$:

Result 1. Consider a spherical function $g(\theta, \phi) = \sum_j g_j(\theta, \phi)$. The rank- j components $g_j(\beta, \alpha)$ for angles β and α can be obtained from the scalar products

$$g_j(\beta, \alpha) = s_j \langle R_{\alpha\beta}Y_{j0}(\theta, \phi) | g(\theta, \phi) \rangle_{L^2} \quad (4)$$

with $s_j := \sqrt{(2j+1)/(4\pi)}$.

Assuming that an operator A is represented by a set of spherical functions $f^{(\ell)}(\theta, \phi)$, we can apply Result 1 by setting $g(\theta, \phi) := f^{(\ell)}(\theta, \phi)$ for each label ℓ separately. We extend Result 1 such that the spherical rank- j components $f_j^{(\ell)}(\beta, \alpha)$ can also be recovered by comparing the operator A directly with rotated axial tensor operators $\mathcal{R}_{\alpha\beta}T_{j0}^{(\ell)}$. Consequently, the values of the rank- j spherical components $f_j^{(\ell)}(\beta, \alpha)$ can be experimentally measured for any combination of polar angles β and azimuthal angles α . Here, $\mathcal{R}_{\alpha\beta}C := \mathfrak{R}_{\alpha\beta}C\mathfrak{R}_{\alpha\beta}^{-1}$ describes the rotation of an n -spin operator C where the simultaneous rotation $\mathfrak{R}_{\alpha\beta} = e^{-i\alpha F_z} e^{-i\beta F_y}$ of all spins is defined using the total spin operators $F_z = \sum_{k=1}^n I_{kz}$ and $F_y = \sum_{k=1}^n I_{ky}$ [16, 41]. We recall the scalar product $\langle C | B \rangle = \text{tr}(C^\dagger B)$ for operators C and B as well as the definition of the expectation value $\langle B \rangle_\rho = \text{tr}(\rho B)$ of an operator B if the state of the spin system is given by the density matrix ρ . Our result for recovering rank- j droplet components of an operator can now be stated as follows:

Result 2. Consider a multi-spin operator A which is represented by a set of spherical functions $f^{(\ell)}(\theta, \phi) = \sum_{j \in J(\ell)} f_j^{(\ell)}(\theta, \phi)$. For each label ℓ , the rank- j component

$f_j^{(\ell)}(\beta, \alpha)$ can be experimentally measured for arbitrary angles β and α via the scalar products

$$f_j^{(\ell)}(\beta, \alpha) = s_j \langle \mathcal{R}_{\alpha\beta} T_{j0}^{(\ell)} | A \rangle. \quad (5)$$

If the density matrix ρ of a spin system can be prepared to be identical to the operator A , the rank- j droplet components are given by the expectation values

$$f_j^{(\ell)}(\beta, \alpha) = s_j \langle \mathcal{R}_{\alpha\beta} T_{j0}^{(\ell)} \rangle_{\rho}. \quad (6)$$

The proofs of Results 1 and 2 are deferred to Appendices A and B. Equation (6) implies that the rank- j droplet components $f_j^{(\ell)}(\beta, \alpha)$ for a density matrix ρ can be calculated from the expectation values of rotated axial tensor operators $\mathcal{R}_{\alpha\beta} T_{j0}^{(\ell)}$. Result 2 shows that one can retrace the shapes of the spherical functions $f^{(\ell)}(\beta, \alpha)$ representing any operator that can be mapped onto the density matrix if one experimentally measures $f^{(\ell)}(\beta, \alpha)$ for sufficiently many angles β and α .

IV. DROPLETS AS MULTIPOLE POTENTIALS

The methodology of Wigner tomography as presented in Sec. III can be motivated by relating spherical functions to physical multipole potentials. Section IV A details connections to dipole potentials, which is then generalized to fictitious multipole potentials in Sec. IV B. This allows us to interpret the proposed Wigner tomography as measuring a fictitious potential using axial multipole sensors (see Sec. IV C).

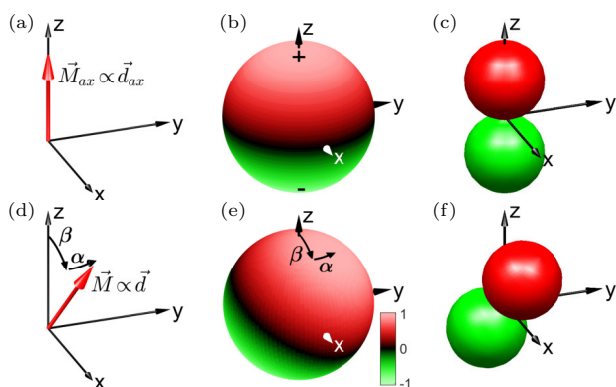


FIG. 2. (Color online) (a) Axial magnetization vector \vec{M}_{ax} and collinear axial dipole vector \vec{d}_{ax} . (b) Corresponding dipole potential visualized on a sphere, with magnitude and sign specified by brightness and color. (c) Similar to panel (b), but with magnitude specified by the distance from the origin. (d-f) Rotated nonaxial dipole \vec{d} [42].

A. Spherical functions and dipole potentials

The most direct physical interpretation of spherical functions is found for Hermitian single-spin terms [16, 41]

$$\rho_k = m_x I_{kx} + m_y I_{ky} + m_z I_{kz} \quad (7)$$

of the density matrix with (possibly time-dependent) real coefficients m_x , m_y , and m_z . The corresponding spherical function $f^{\{k\}}(\theta, \phi)$ is now related to a magnetic dipole potential. The operator ρ_k associated with spin k is interpreted as a magnetization vector (or Bloch vector) $\vec{M} = (m_x, m_y, m_z)^T$ the components of which are proportional to the expectation values of the spin operators I_{kx} , I_{ky} , and I_{kz} . An actual (time-dependent) magnetic dipole $\vec{d} \propto \vec{M}$ creates a detectable signal in an NMR experiment by inducing a voltage in a detection coil. It is associated with a scalar dipole potential $V_1(\vec{r})$ at $\vec{r} = |\vec{r}|(\sin\theta \cos\phi, \sin\theta \sin\phi, \cos\theta)$, where θ and ϕ are polar and azimuthal angles, respectively. At a constant distance $|\vec{r}|$ from the dipole, the potential $V_1(\vec{r})$ is proportional to the scalar product $\vec{d} \cdot \vec{r}$ [38]. In the case of an axial dipole $\vec{d}_{ax} \propto (0, 0, 1)^T$ oriented along the z axis, the dipole potential is proportional to the axial spherical harmonic $Y_{10}(\theta, \phi) = \sqrt{3}/(4\pi) \cos\theta$ as detailed in Fig. 2(a)-(c). For a general dipole $\vec{d} = R_{\alpha\beta} \vec{d}_{ax} \propto (\sin\beta \cos\alpha, \sin\beta \sin\alpha, \cos\beta)^T$, the dipole potential $V_1(\vec{r}) \propto R_{\alpha\beta} Y_{10}(\theta, \phi)$ is rotated accordingly as shown in Fig. 2(d)-(f). Recall that $R_{\alpha\beta}$ denotes a rotation around the y axis by a polar angle β followed by one around the z axis by an azimuthal angle α .

A scalar dipole potential $V_1(\vec{r}) = V_1(\theta, \phi)$ can be indicated by its values on the surface of a sphere by encoding its sign by the color and its magnitude by the brightness [see Fig. 2(b) and (e)]. Alternatively, its magnitude can be represented by the distance from the origin as in Fig. 2(c) and (f), where dipole potentials are shown as a positive, red (dark gray) sphere and a negative, green (light gray) one which touch each other at the origin. This characteristic shape arises as $V_1(\theta, \phi)$ is proportional to the projection of the dipole \vec{d} onto \vec{r} as depicted in Fig. 3. Also, the vector from the center of the negative sphere to the positive one is collinear with \vec{d} .

In summary, a single-spin axial spherical tensor operator $T_{10}^{\{k\}} = \sqrt{2} I_{kz}$ is mapped to the axial spherical harmonics $Y_{10}(\theta, \phi)$, and ρ_k from Eq. (7) is mapped to

$$f^{\{k\}}(\theta, \phi) = |\vec{M}| R_{\alpha\beta} Y_{10}(\theta, \phi) / \sqrt{2}, \quad (8)$$

where $\beta = \text{atan}(m_z / \sqrt{m_x^2 + m_y^2})$, $\alpha = \text{atan}(m_y / m_x)$, and $|\vec{M}| = \sqrt{m_x^2 + m_y^2 + m_z^2}$. Although the direct correspondence between spherical functions and actual physical dipole potentials appears to be limited to the case of single-spin terms, it suggests the following interpretation for other spherical functions presented here.

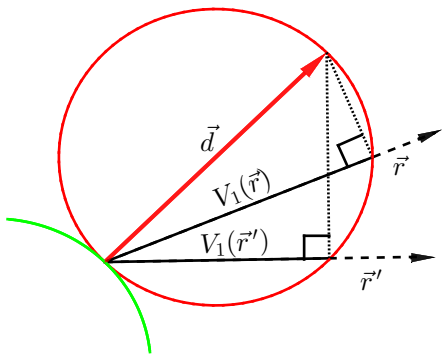


FIG. 3. (Color online) Slice of Fig. 2(f): dipole potential $V_1(\vec{r})$ proportional to scalar product $\vec{d} \cdot \vec{r}$ (projection of \vec{d} onto \vec{r}) due to Thales' theorem, and similar for \vec{r}' , results are shown in positive (red) and negative (green) spheres in Fig. 2(f); for $\angle\{\vec{d}, \vec{r}\} > 90$ deg, the negative scalar product leads to the negative sphere.

B. Fictitious multipole potentials

Any spherical function $f^{(\ell)}(\theta, \phi)$ can be regarded as the potential $V^{(\ell)}(\vec{r})$ of a fictitious charge distribution $\sigma^{(\ell)}(\vec{r})$ localized in a small volume close to the origin, i.e., $\sigma^{(\ell)}(\vec{r})$ is non-zero only for $|\vec{r}| \ll 1$. At a radius of $|\vec{r}| = 1$, the potential can be expressed as a sum $V^{(\ell)}(\theta, \phi) = \sum_j V_j^{(\ell)}(\theta, \phi)$ of different 2^j -pole potentials $V_j^{(\ell)}(\theta, \phi)$. Although a large number of multipole potentials might be required in general, only a moderate number of components with different rank j appear for up to three spins in the DROPS representation of Sec. II [30]. Fictitious multipole potentials sufficient to completely describe the potential $V^{(\ell)}(\theta, \phi)$ are detailed in Table I: one has monopoles ($2^0 = 1$), dipoles ($2^1 = 2$), quadrupoles ($2^2 = 4$), and octupoles ($2^3 = 8$). For a two-spin droplet with label “ $\{kl\}$ ”, only ranks j of zero, one, and two occur which correspond to fictitious monopole, dipole, and quadrupole potentials, whereas the fully symmetric three-spin droplet with label “ $\{123\}, \tau_1$ ” has only rank-1 and rank-3 components associated with dipole and octupole terms.

C. Axial multipole sensors

Based on the provided interpretation of droplet functions as fictitious multipole potentials, the results of Sec. III on how to experimentally measure spherical functions of spin operators can be mapped to the analogous problem of measuring an unknown electrostatic potential. This analogy is complete for Hermitian spin operators with real-valued spherical functions [30]. Suppose we would like to determine an unknown (real-valued) electrostatic potential $V(\theta, \phi)$ at a radius $|\vec{r}| = 1$ that is created by an object located in the interior of a unit sphere. An electric point charge q at position \vec{r} in an electric

TABLE I. Number n of involved spins, components $A^{(\ell)}$ and $f^{(\ell)}$, possible ranks j , rank- j contributions $A_j^{(\ell)}$ and $f_j^{(\ell)}$, as well as 2^j -pole potentials $V_j^{(\ell)}$ are listed for up to three spins 1/2 and all labels (ℓ) ; k and l indicate the involved spins [30].

n	$A^{(\ell)}$	$f^{(\ell)}$	j	$A_j^{(\ell)}$	$f_j^{(\ell)}$	2^j	2^j -pole	$V_j^{(\ell)}$
0	A^0	f^0	0	A_0^0	f_0^0	1	monopole	V_0^0
1	$A^{\{k\}}$	$f^{\{k\}}$	1	$A_1^{\{k\}}$	$f_1^{\{k\}}$	2	dipole	$V_1^{\{k\}}$
2	$A^{\{kl\}}$	$f^{\{kl\}}$	0	$A_0^{\{kl\}}$	$f_0^{\{kl\}}$	1	monopole	$V_0^{\{kl\}}$
			1	$A_1^{\{kl\}}$	$f_1^{\{kl\}}$	2	dipole	$V_1^{\{kl\}}$
			2	$A_2^{\{kl\}}$	$f_2^{\{kl\}}$	4	quadrupole	$V_2^{\{kl\}}$
3	A^{τ_1}	f^{τ_1}	1	$A_1^{\tau_1}$	$f_1^{\tau_1}$	2	dipole	$V_1^{\tau_1}$
			3	$A_3^{\tau_1}$	$f_3^{\tau_1}$	8	octupole	$V_3^{\tau_1}$
	A^{τ_2}	f^{τ_2}	1	$A_1^{\tau_2}$	$f_1^{\tau_2}$	2	dipole	$V_1^{\tau_2}$
			2	$A_2^{\tau_2}$	$f_2^{\tau_2}$	4	quadrupole	$V_2^{\tau_2}$
	A^{τ_3}	f^{τ_3}	1	$A_1^{\tau_3}$	$f_1^{\tau_3}$	2	dipole	$V_1^{\tau_3}$
			2	$A_2^{\tau_3}$	$f_2^{\tau_3}$	4	quadrupole	$V_2^{\tau_3}$
	A^{τ_4}	f^{τ_4}	0	$A_0^{\tau_4}$	$f_0^{\tau_4}$	1	monopole	$V_0^{\tau_4}$

potential $V(\vec{r})$ has a potential energy $U_{pot}(\vec{r}) = qV(\vec{r})$. Given an electrostatic potential $V(\theta, \phi)$, the electrostatic potential energy of a (nonconducting) unit sphere with the surface charge distribution $\sigma(\theta, \phi)$ is given by

$$U_{pot}(\beta, \alpha) = \int_{\theta=0}^{\pi} \int_{\phi=0}^{2\pi} \sigma(\theta, \phi) V(\theta, \phi) \sin \theta d\theta d\phi, \quad (9)$$

which is equivalent to $U_{pot}(\beta, \alpha) = \langle \sigma(\theta, \phi) | V(\theta, \phi) \rangle_{L^2}$ for real valued $\sigma(\theta, \phi)$ as in Eq. (4) of Sec. III.

The 2^j -pole components $V_j(\theta, \phi)$ of an unknown multipole potential $V(\theta, \phi)$ can be sampled by a set of axial 2^j -pole sensors, each consisting of a charge distribution $\sigma_{j0}(\theta, \phi)$ proportional to the axial spherical harmonics $Y_{j0}(\theta, \phi)$. Each individual sample $V_j(\beta, \alpha)$ can be determined using Eq. (9) by measuring the potential energy

$$V_j(\beta, \alpha) \propto U_{pot}(\beta, \alpha) = \langle R_{\alpha\beta} \sigma_{j0}(\theta, \phi) | V(\theta, \phi) \rangle$$

of the axial 2^j -pole sensor rotated by the polar angle β around the y axis followed by a rotation by the azimuthal angle α around the z axis. The full electrostatic 2^j -pole potential $V_j(\theta, \phi)$ can be recovered by systematically incrementing β and α . In summary, the analogy between real-valued spherical functions and multipole potentials helps to better understand our results of Sec. III on the measurement of spherical functions. It can also be extended in a straight-forward manner to non-Hermitian spin operators by considering complex, fictitious multipole potentials.

TABLE II. Root-mean-square error of the experimental reconstruction for the prepared Cartesian product operators on one-, two-, and three-spin systems; $I_{abc} := I_{1a}I_{2b}I_{3c}$.

spins	prod. op.	error	spins	prod. op.	error
1	I_x	0.0519	3	$4I_{xxx}$	0.0797
	I_y	0.1187		$4I_{yyy}$	0.0509
	I_z	0.0356		$4I_{xyz}$	0.0617
2	$2I_{1x}I_{2x}$	0.0173	$4I_{xyy}$	0.0395	
	$2I_{1y}I_{2y}$	0.0154	$4I_{yxy}$	0.0476	
	$2I_{1z}I_{2z}$	0.0850	$4I_{yyx}$	0.0954	
	$2I_{1x}I_{2y}$	0.0487	$4I_{xxy}$	0.0587	
	$2I_{1y}I_{2x}$	0.0152	$4I_{xyx}$	0.0638	
	$2I_{1z}I_{2x}$	0.0319	$4I_{yxx}$	0.0692	

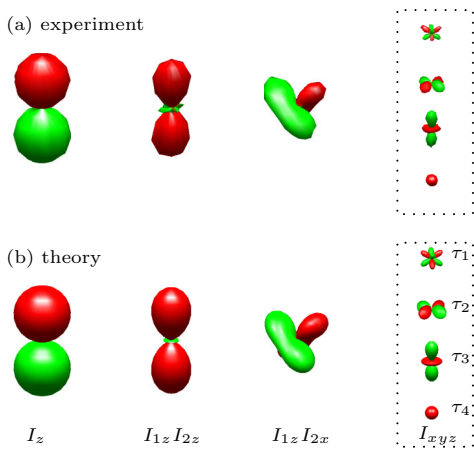


FIG. 4. (Color online) Spherical functions from (a) experiment and (b) theory; $I_{xyz} := I_{1x}I_{2y}I_{3z}$ splits into f^{τ_1} , f^{τ_2} , f^{τ_3} , and f^{τ_4} (see Fig. 1) [42]. Further examples are shown in Figs. 5 and 6.

V. SUMMARY OF NMR EXPERIMENTS

Building on the previous sections, we demonstrate the Wigner tomography of various prepared density-matrix components in spin-1/2 systems using nuclear magnetic resonance. Experimental details are deferred to Secs. VII and VIII where the precise experimental scheme and its implementation on a spectrometer are discussed. The experiments were performed on one-, two-, and three-spin systems. The shapes of the spherical functions are recovered for the prepared Cartesian products operators listed in Table II, where also their respective experimental reconstruction errors are given. Experimental and theoretical results for the reconstruction are visually compared for four examples in Fig. 4. For the rightmost example of $4I_{1x}I_{2y}I_{3z}$ in Fig. 4, multiple droplets corresponding to different permutation symmetries are necessary to completely describe the quantum operator, as outlined in Sec. II (see Fig. 1 and [30]).

VI. TEMPORAL AVERAGING

Re-using our experimental data as summarized in Sec. V, we can also highlight how temporal averaging [45] is used to emulate the preparation of quantum operators. The direct experimental preparation of Hermitian operators would be also possible, but we have chosen temporal averaging for its simplicity and convenience. The experimental values are shown in Fig. 5, while the corresponding theoretical predictions are given in Fig. 6. The Cartesian operators $2I_{1x}I_{2x}$, $2I_{1y}I_{2y}$, $2I_{1x}I_{2y}$, and $2I_{1y}I_{2x}$ had been sequentially measured and are now combined in Fig. 5(a) to form the double quantum operators

$$\text{DQ}_x := I_{1x}I_{2x} - I_{1y}I_{2y} \quad \text{and} \quad \text{DQ}_y := I_{1x}I_{2y} + I_{1y}I_{2x}.$$

Their characteristic shapes reflect the fact that they have coherence order $|p| = 2$ and are invariant under non-selective rotations around the z axis by an integer multiple of 180 deg [30]. This is in contrast to single-quantum operators such as the linear operators I_x or I_y [see 5(c)] or the bilinear operator $2I_{1z}I_{2x}$ [see Fig. 4] which are only invariant under non-selective rotations around the z axis by an integer multiple of 360 deg [16].

In general, $|p|$ -quantum operators are invariant under non-selective rotations around the z axis by an integer multiple of $360/|p|$ deg, and their spherical functions illustrate this symmetry. Figure 5(b) exemplifies the invariance under 120 deg rotations around the z axis in the case of $|p| = 3$ for the triple-quantum operator

$$\text{TQ}_x := I_{1x}I_{2x}I_{3x} - I_{1x}I_{2y}I_{3y} - I_{1y}I_{2x}I_{3y} - I_{1y}I_{2y}I_{3x},$$

similar to the case of

$$\text{TQ}_y := I_{1y}I_{2x}I_{3x} + I_{1x}I_{2y}I_{3x} + I_{1x}I_{2x}I_{3y} - I_{1y}I_{2y}I_{3y}.$$

Up to experimental imperfections, only the spherical function f^{τ_1} contributes to the operator TQ_x .

Finally, we also consider temporal averaging for non-Hermitian operators which obviously cannot be directly prepared in experiments (see also Sec. VII). Figure 5(c) presents the non-Hermitian operators $I_1^+ = I_x + iI_{2y}$, $I_1^+I_2^+ = \text{DQ}_x + i\text{DQ}_y$, and $I_1^+I_2^+I_3^+ = \text{TQ}_x + i\text{TQ}_y$. These operators have the respective coherence orders p of 1, 2, and 3 which results in donut-shaped spherical functions the colors of which cycle through one, two, or three rainbows [30].

VII. WIGNER TOMOGRAPHY USING NMR

We complement our results in Sec. III and describe the experimental scheme for an NMR-based implementation of our Wigner tomography. Recall that Eq. (5) of Result 2 provides an approach for measuring an arbitrary operator. This can be translated into the diagram of

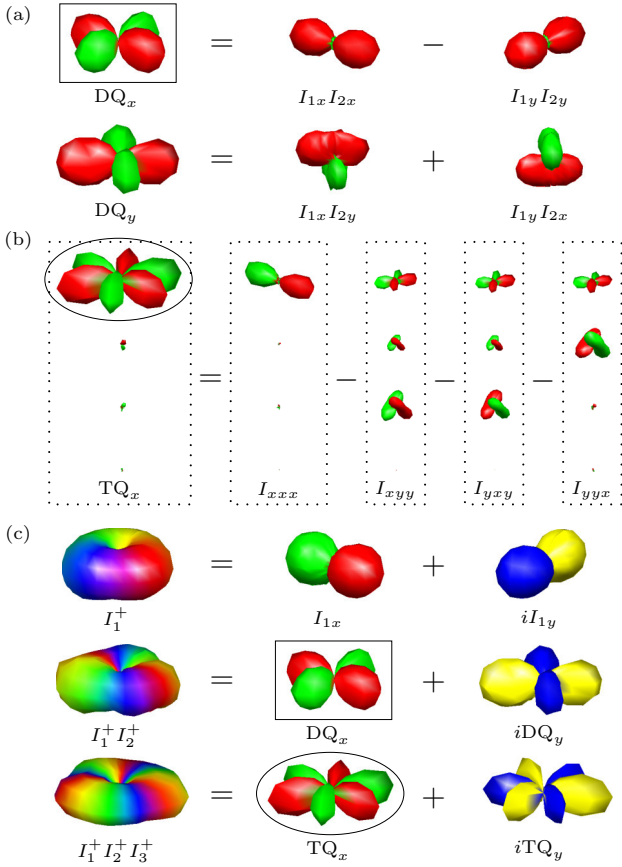


FIG. 5. (Color online) Temporal averaging: decomposition of (a) DQ_x [box, see also panel (c)], DQ_y , and (b) TQ_x [f^{τ_1} ellipse, see also panel (c)], $I_{abc} := I_{1a}I_{2b}I_{3c}$. (c) non-Hermitian operators I_1^+ , $I_1^+I_2^+$, and $I_1^+I_2^+I_3^+$ as complex linear combination of Hermitian ones (see Fig. 4).

Fig. 7(a): The operator A is decomposed into its components $A_j^{(\ell)}$ which are mapped by the Wigner transformation W to spherical samples $f_j^{(\ell)}(\beta, \alpha)$. The spherical samples can be recovered using Eq. (5). Very similarly, Fig. 7(b) depicts the equivalent measurement procedure for density matrices which relies on Eq. (6) of Result 2.

Before proceeding to the NMR-based scheme, it is important to emphasize that only traceless operators can be measured in NMR experiments [16], which rules out the identity component of a density matrix. However, the traceless part of a density matrix covers most important features, and it is sufficient to calculate the time evolution and all relevant expectation values. Hence, we will consider in the following only the traceless part which is for simplicity also denoted by ρ .

Further complications arise from the fact that signatures of Cartesian product operators [16] that contain only a single transverse Cartesian operator I_{ka} with $a \in \{x, y\}$ can be measured *directly*; examples are I_{ka} , $2I_{ka}I_{lz}$, and $4I_{ka}I_{lz}I_{mz}$. This complication can be resolved in two steps: Firstly, any traceless operator can

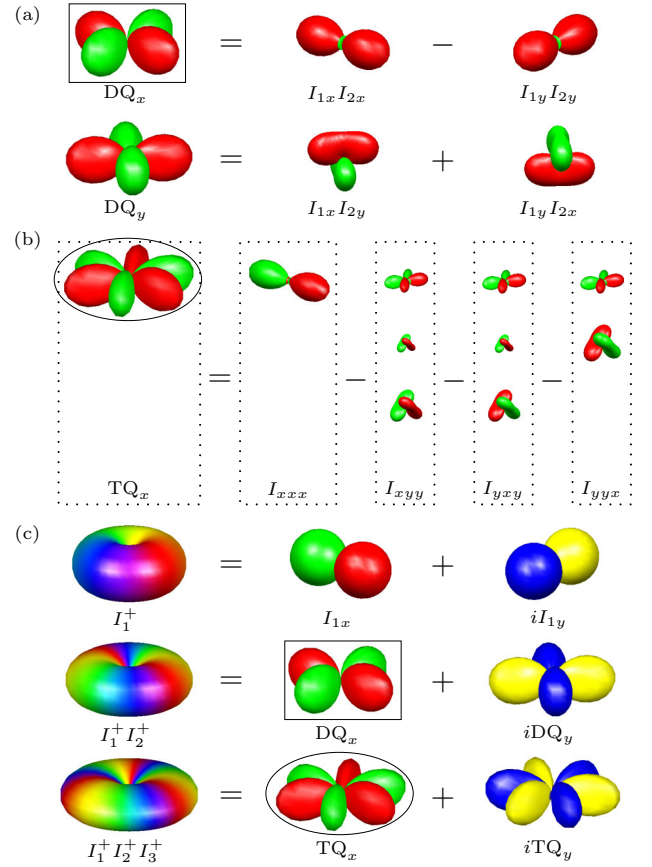


FIG. 6. (Color online) Theoretical predictions corresponding to Fig. 5; $I_{abc} := I_{1a}I_{2b}I_{3c}$.

be decomposed into (Hermitian) Cartesian product operators $C_j^{(\ell, n)}$. This decomposition of relevant axial tensors

$$T_{j_0}^{(\ell)} = \sum_n r_j^{(\ell, n)} C_j^{(\ell, n)} \quad (10)$$

with respect to real coefficients $r_j^{(\ell, n)}$ is given in Table III.

For example, the axial tensor operator $T_{10}^{\{k\}}$ acting on the k th spin decomposes directly into the Cartesian product operator $C_1^{\{k, 1\}} = I_{kz}$ with the coefficient $r_1^{\{k, 1\}} = \sqrt{2}$.

Secondly, the Cartesian product operators have to be transformed into NMR-measurable ones

$$M_j^{(\ell, n)} = U_j^{(\ell, n)} C_j^{(\ell, n)} U_j^{(\ell, n)\dagger}. \quad (11)$$

The unitary operators $U_j^{(\ell, n)}$ can be experimentally realized using radio-frequency pulses and evolution periods under couplings as discussed in Sec. VIII B and their explicit form is detailed in App. D. Combining both steps leads to an *indirect* approach for measuring spherical functions of density operators, as schematically outlined in Fig. 7(c). The density matrix is equivalently rotated inversely in contrast to Fig. 7(a)-(b) where the axial tensor operator $T_{j_0}^{(\ell)}$ is rotated. The complete measurement scheme is formalized along the lines of Result 2:

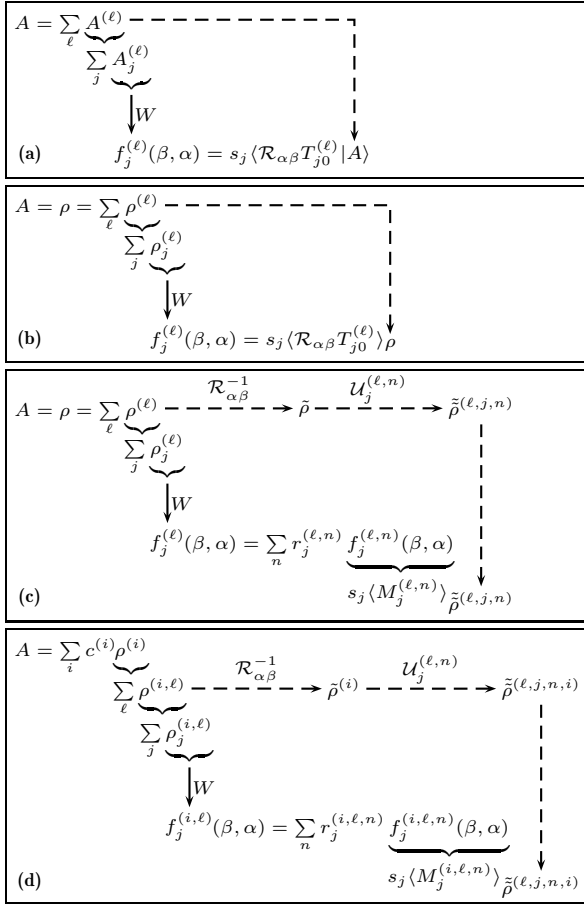


FIG. 7. Sampling schemes for spherical functions using (a) scalar products of rotated axial tensor operators and A [Result 2, Eq. (5)]. (b) Expectation values of rotated axial tensor operators w.r.t. ρ [Result 2, Eq. (6)]. (c) Experimentally measurable expectation values as in panel (b) [Result 3, Eqs. (12)-(14)]. (d) non-Hermitian operators averaged as complex combinations of Hermitian terms $\rho^{(i)}$ [see Eq. (15)]. The Wigner transformation W maps an operator to its spherical function.

Result 3. Consider a density operator ρ which is represented by a set of spherical functions $f^{(\ell)}(\theta, \phi) = \sum_{j \in J(\ell)} f_j^{(\ell)}(\theta, \phi)$. For each label ℓ , the rank- j component $f_j^{(\ell)}(\beta, \alpha)$ can be measured for arbitrary angles β and α by determining the expectation values

$$f_j^{(\ell)}(\beta, \alpha) = s_j \sum_n r_j^{(\ell,n)} \langle M_j^{(\ell,n)} \rangle_{\tilde{\rho}^{(\ell,j,n)}} \quad (12)$$

of suitable operators $M_j^{(\ell,n)}$ as in Eq. (11), where

$$\tilde{\rho}^{(\ell,j,n)} = U_j^{(\ell,n)} \tilde{\rho} = U_j^{(\ell,n)} \tilde{\rho} U_j^{(\ell,n)\dagger}, \quad (13)$$

$$\tilde{\rho} = \mathcal{R}_{\alpha\beta}^{-1} \rho = \mathfrak{R}_{\alpha\beta}^{-1} \rho \mathfrak{R}_{\alpha\beta}, \quad (14)$$

and $\mathfrak{R}_{\alpha\beta} = \exp(-i\alpha \sum_{k=1}^n I_{kz}) \exp(-i\beta \sum_{k=1}^n I_{ky})$.

TABLE III. Axial tensor operators $T_{j0}^{(\ell)}$ and their decomposition into Cartesian product operators $C_j^{(\ell,n)}$ for three spins [30].

$T_{j0}^{(\ell)}$	$\sum_n r_j^{(\ell,n)} C_j^{(\ell,n)}$
$T_{10}^{\{k\}}$	$\sqrt{2} I_{kz}$
$T_{00}^{\{kl\}}$	$(2I_{kx}I_{lx} + 2I_{ky}I_{ly} + 2I_{kz}I_{lz})/\sqrt{3}$
$T_{10}^{\{kl\}}$	$(2I_{kx}I_{ly} - 2I_{ky}I_{lx})/\sqrt{2}$
$T_{20}^{\{kl\}}$	$[-2I_{kx}I_{lx} - 2I_{ky}I_{ly} + 2(2I_{kz}I_{lz})]/\sqrt{6}$
$T_{10}^{\tau_1}$	$\sqrt{8}(I_{xxz} + I_{xzx} + I_{zxx} + I_{yyz} + I_{yzy} + I_{zyy} + 3I_{zzz})/\sqrt{15}$
$T_{30}^{\tau_1}$	$-2(I_{xxz} + I_{xzx} + I_{zxx} + I_{yyz} + I_{yzy} + I_{zyy} - 2I_{zzz})/\sqrt{5}$
$T_{10}^{\tau_2}$	$\sqrt{2}[-2(I_{xxz} + I_{yyz}) + I_{zxx} + I_{xzx} + I_{zyy} + I_{yzy}]/\sqrt{3}$
$T_{20}^{\tau_2}$	$\sqrt{2}(I_{yzx} + I_{zyx} - I_{xzy} - I_{zxy})$
$T_{10}^{\tau_3}$	$\sqrt{2}(I_{zxx} - I_{xzx} + I_{zyy} - I_{yzy})$
$T_{20}^{\tau_3}$	$\sqrt{2}[-2(I_{xyz} - I_{yxz}) + I_{zxy} - I_{xzy} + I_{yzz} - I_{zyx}]/\sqrt{3}$
$T_{00}^{\tau_4}$	$2(I_{xyz} - I_{xzy} - I_{yxz} + I_{yzz} + I_{zxy} - I_{zyx})/\sqrt{3}$

A detailed derivation of Eq. (12) is provided in Appendix C. In summary, the rank- j components $f_j^{(\ell)}$ of spherical functions $f^{(\ell)}$ representing the density matrix ρ can be sampled in NMR experiments by transforming the density operator ρ to the states $\tilde{\rho}^{(n)}$ and then measuring a set of expectation values of suitable operators $\langle M_j^{(\ell,n)} \rangle_{\tilde{\rho}^{(\ell,j,n)}}$. The explicit form of the Cartesian operators $C_j^{(\ell,n)}$, their NMR-measurable forms $M_j^{(\ell,n)}$, and the transformations $U_j^{(\ell,n)}$ for up to three spins is given in App. D.

The approach of Result 3 can be extended to non-Hermitian operators, even though these cannot be prepared directly in an experiment. We apply temporal averaging [45] as already discussed in Sec. VI. Any operator A can be expressed as a complex linear combination $A = \sum_i c^{(i)} \rho^{(i)}$ of Hermitian operators $\rho^{(i)}$. As the DROPS representation is linear, we can sample the traceless part of any operator A using the spherical functions

$$\begin{aligned} f_j^{(\ell)}(\beta, \alpha) &= \sum_i c^{(i)} f_j^{(i,\ell)}(\beta, \alpha) \\ &= \sum_i c^{(i)} s_j \langle \mathcal{R}_{\alpha\beta} T_{j0}^{(\ell)} \rangle_{\rho^{(i)}} \\ &= \sum_i c^{(i)} s_j \sum_n r_j^{(\ell,n)} \langle M_j^{(\ell,n)} \rangle_{\tilde{\rho}^{(\ell,j,n,i)}}. \end{aligned} \quad (15)$$

In an experiment, temporal averaging of Hermitian operators $\rho^{(i)}$ can be implemented by sequentially measuring spherical functions for each operator $\rho^{(i)}$ and linearly combining the results $f_j^{(i,\ell)}(\beta, \alpha) = s_j \langle \mathcal{R}_{\alpha\beta} T_{j0}^{(\ell)} \rangle_{\rho^{(i)}} = s_j \sum_n r_j^{(\ell,n)} \langle M_j^{(\ell,n)} \rangle_{\tilde{\rho}^{(\ell,j,n,i)}}$ as illustrated in Fig. 7(d).

VIII. EXPERIMENTAL IMPLEMENTATION

After outlining the experimental scheme for Wigner tomography in Sec. VII, we present now the details for the experimental implementation which results in the spherical functions in Figs. 4-5. We start by describing the molecules and experimental setting in Sec. VIII A. We continue in Sec. VIII B with the experimental protocol, and we finally discuss experimental errors in Sec. VIII C.

A. Molecules and experimental setting

In order to simplify the experiments, the linear and bilinear Cartesian product operators have been prepared and measured using respective single-spin and two-spin samples: The single-spin sample was prepared by dissolving 5% H₂O in D₂O, which resulted in a sample containing about 10% HDO, i.e. water molecules in which one of the ¹H spins is replaced by deuterium (²D) [see Fig. 8(a)]. In case of two spins, we have used a 10% sample of chloroform dissolved in fully deuterated DMSO-d₆, where the ¹H spin and the ¹³C spin of each chloroform molecule form a system consisting of two coupled heteronuclear spins 1/2 [see Fig. 8(b)]. A three-spin sample consisting of 2-¹³C-2-fluoromalonic-acid-diethyl-ester dissolved in CD₃CN [see Fig. 8(c)] was utilized for the preparation and reconstruction of trilinear operators. All liquid samples were measured in 5 mm Shigemi NMR tubes at room temperature (298 K) in a 14.1 T magnet using a Bruker Avance III 600 spectrometer.

B. Experimental protocol

Our experimental protocol is composed of five main building blocks (see Fig. 9). In the first block \mathcal{P} , the desired density operator ρ is prepared starting from the initial thermal equilibrium density operator which in the high-temperature limit is proportional to [16] $\rho_{th} = \sum_{k=1}^N \gamma_k I_{kz}$, where γ_k denotes the gyromagnetic ratio of the k th nuclear spin. This requires unitary transformations which are created by pulses and evolution periods under the effect of couplings and frequency offsets as well as non-unitary transformations which are implemented by pulsed magnetic-field gradients. The explicit pulse sequences are discussed in App. D. Table II in Sec. V summarizes all the different Cartesian product operators which have been experimentally prepared.

The second block consists of the rotation $\mathcal{R}_{\alpha_r, \beta_r}^{-1}$ which rotates the prepared density operator ρ into $\tilde{\rho}$ in order to probe the corresponding spherical functions $f_j^{(\ell)}(\beta_r, \alpha_r)$ for different polar angles β_r and azimuthal angles α_r using axial tensor operators, i.e., axial multipole sensors) (see Result 3). The rotation $\mathcal{R}_{\alpha_r, \beta_r}^{-1}$ is implemented by rf pulses $[\beta_r]_{\alpha_r, -\pi/2}$ with flip angle β_r and phase $(\alpha_r - \pi/2)$ which are simultaneously applied to all spins.

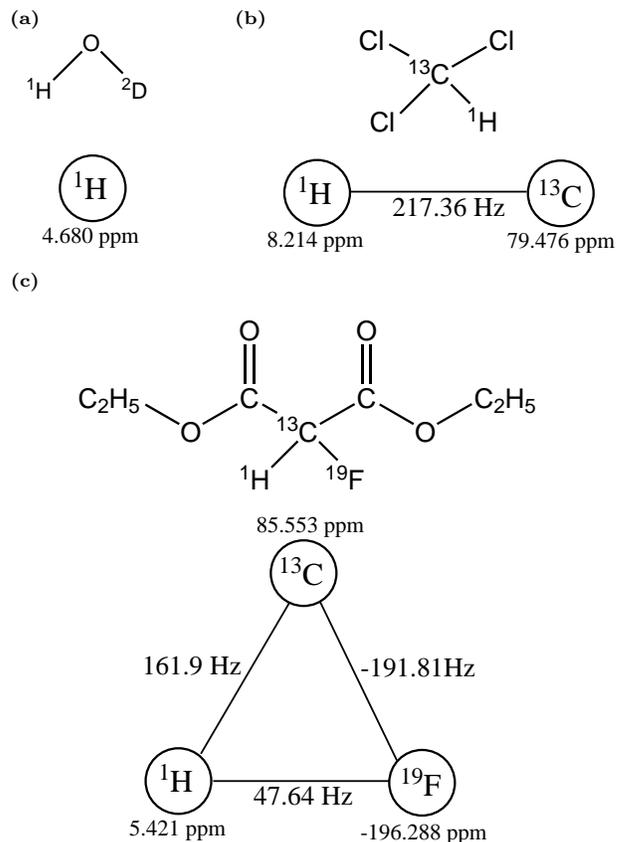


FIG. 8. Molecules (a) HDO, (b) chloroform, and (c) 2-¹³C-2-fluoromalonic-acid-diethyl-ester used in experiments with their schematic spin systems and coupling topologies; individual spins are labeled by chemical shifts (in parts per million); heteronuclear J couplings (lines) are labeled by coupling constants J_{kl} (in hertz).

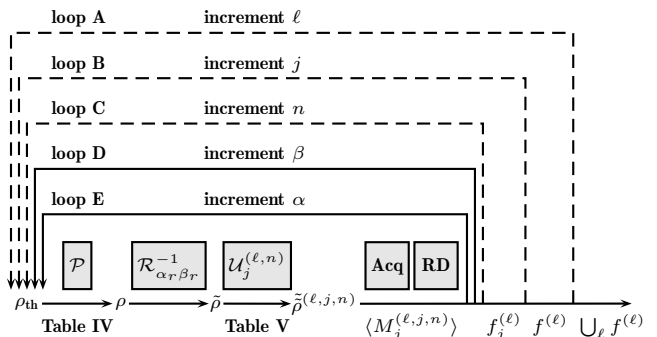


FIG. 9. Tomography scheme proposed by Result 3; note that $\langle M_j^{(\ell, j, n)} \rangle := \langle M_j^{(\ell, j, n)} \rangle_{\tilde{\rho}^{(\ell, j, n)}}$.

The unitary transformations $\mathcal{U}_j^{(\ell, n)}$ [see Eq. (13) of Result 3] are applied in the third block in order to transform the density matrix $\tilde{\rho}$ into directly detectable Cartesian product operators for the various linear, bilinear, and trilinear operators (see Table III in Sec. VII). The specific experimental implementation of the unitary transforma-

tions $\mathcal{U}_j^{(\ell,n)}$ consists of rf pulses with flip angle $\pi/2$ as detailed in App. D.

In the fourth block, the NMR signal is measured in an acquisition period Acq which has a duration of 5.7 ms (one spin), 11.4 ms (two spins), and 14.9 ms (three spins). In the last block, a relaxation delay RD with a duration of 7 s (one spin), 10 s (two spins), and 15 s (three spins) recovers the initial equilibrium state ρ_{th} ,

In the tomography experiment, all blocks are repeated multiple times (see Fig. 9). The outer loop A runs over all possible droplets $\ell \in L$. Loop B runs over all ranks j contributing to the droplet ℓ . Loop C cycles through all Cartesian product operators $C_j^{(\ell,n)}$ [see Eq. (10)] appearing in the decomposition of the axial tensor operator $T_{j0}^{(\ell)}$ (see Table III in Sec. VII). Finally, the discretized angles $\beta_r \in \{0, 15, 30, \dots, 180\}$ and $\alpha_r \in \{0, 15, 30, \dots, 360\}$ (both in degrees) are incremented in the innermost loops D and E. Although not explicitly indicated in Fig. 9, one further loop is necessary for a temporal averaging scheme [see Eq. (15)].

The whole protocol allows us to determine expectation values $\langle M_j^{(\ell,n)} \rangle_{\tilde{\rho}^{(\ell,j,n)}}$, which are normalized and range between 1 and -1 . As illustrated in Fig. 10, the spherical functions $f^{(\ell)}(\theta, \phi)$ can be reconstructed by plotting the spherical samples $f^{(\ell)}(\beta_r, \alpha_r)$ for all angles $\beta_r \in \{0, \dots, \pi\}$ and $\alpha_r \in \{0, \dots, 2\pi\}$ at a distance $|f^{(\ell)}(\beta_r, \alpha_r)|$ from the origin. The phase $\varphi^{(\ell)}(\beta_r, \alpha_r) = \text{atan}(\text{Im}\{f^{(\ell)}(\beta_r, \alpha_r)\}/\text{Re}\{f^{(\ell)}(\beta_r, \alpha_r)\})$ is color coded. For example, the spherical function of the Hermitian operator I_{1x} is given by a real function, and the positive and negative values of $f^{(\ell)}(\theta, \phi)$ are indicated by the colors red (dark gray) and green (light gray), respectively.

C. Experimental errors

A reasonable match between the experimentally reconstructed and theoretical predicted spherical functions is found in Figs. 4-6. Deviations are attributed to experimental imperfections, such as the finite experimental signal-to-noise ratio, finite accuracy of pulse calibration, B_0 and B_1 inhomogeneity [16, 46], pulse shape distortions due to the amplifiers and the finite bandwidth of the resonator [47], relaxation losses during the preparation and detection blocks, partial saturation of the signal due to a finite relaxation period between scans, radiation damping effects [48], and truncation effects in the automated integration and comparison of the spectra. We quantify these deviations by the root-mean-square difference between experiment and theory averaged over all measured angles β_r and α_r . The resulting errors for the prepared and measured Cartesian product operators are summarized in Table II of Sec. VII. In order to minimize the effects of field inhomogeneities, Shigemi tubes were used in the experiments in order to reduce the sample volume. We have tested replacing the simple rectangular pulses $[\beta_r]_{\alpha_r - \pi/2}$ in the implementation of the rotations

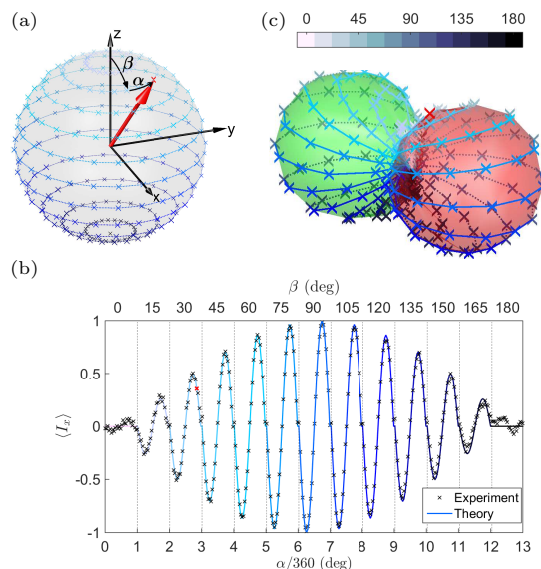


FIG. 10. (Color online) Reconstruction of a spherical function from experimental samples $f^{(\ell)}(\beta_r, \alpha_r)$. (a) Samples (crosses) with different polar angles $\beta_r \in \{0, 180\}$ in degrees (circles colored by latitude) and phases $\alpha_r \in \{0, 360\}$ in degrees acquired using rf-pulses $[\beta_r]_{\alpha_r - \pi/2}$. (b) Predicted expectation values $\langle M_1^{(1,1)} \rangle_{\tilde{\rho}^{(\ell,j,n)}} = \langle I_{1x} \rangle$ depending on a discrete set of polar angles $\beta \in \{0, 15, \dots, 180\}$ in degrees and a continuous set of azimuthal angles α . (c) Smooth surface interpolated from individual samples, distance from the origin given by $f^{(\ell)}(\beta_r, \alpha_r)$ whose phase determines the color of the surface (see Fig. 1).

$\mathcal{R}_{\alpha_r \beta_r}^{-1}$ with composite pulses [49], which, however, did not result in an improved performance.

IX. CONCLUSION

We have theoretically developed and experimentally demonstrated a Wigner tomography scheme the mapping of which multi-spin operators and spherical functions is based on [30]. Our approach reconstructs the relevant spherical functions by measuring expectation values of rotated axial tensor operators, i.e. axial multipole sensors. It is universally applicable and not restricted to NMR methodologies or particles with spin 1/2. A reasonable match between theoretical predictions and NMR experiments was found.

Our theoretical analysis provides a simple physical interpretation of the individual spherical functions in terms of fictitious multipole potentials which can be sampled locally. The objective was to experimentally recover the three-dimensional shapes of the spherical functions for each of the prepared operators. In particular, we have not used any *a priori* information on what shapes to expect. A large number of sampling points is necessary to recover the shapes in sufficient detail. As the simple rectangular grid of sampling points in the space of po-

lar and azimuthal angles used here is highly anisotropic (i.e. more densely concentrated at the poles), a straightforward improvement is to choose more isotropic sampling strategies such as Lebedev grids [50–52]. Moreover, one could use interpolation methods or even adaptive sampling schemes which increase the sampling density in areas where the spherical function varies more strongly. A more quantitative analysis of the complexity of our proposed tomography approach in terms of the number of individual measurements could rely first on a detailed empirical account on how the precision measured by the fidelity depends on the sampling strategy and its density. From the theoretical side, it is clear that the number of measurements for any complete tomography of a quantum state will scale exponentially in the number of qubits (or spins). However, relevant information can be reconstructed in our approach even from a subset of the droplets as discussed under (c) in Sec. II. A more accurate understanding of concrete sampling schemes and their optimization building on our reconstruction method will have to be addressed in future work.

Beyond the optical tomographic methods mentioned at the start of the introduction, tomographic approaches play obviously an important part in almost any experiment in quantum information or quantum physics in general. We will now shortly discuss some selected results from the literature. The proposed reconstruction procedure for spherical functions can be directly extended to other types of spherical representations such as multipole operators [30] or the so-called PROPS representation which is based on products of single-spin representations [53]. Our scheme can also be compared to [54] which introduces Wigner functions built from products of single-spin representations, and a corresponding raster scan method in [55] utilizes the probability to find the rotated system in each of the basis states of a Stern-Gerlach-type experiment. In [56], a similar tomographic method based on filtered back projections (in analogy to planar inverse Radon transforms used e.g. in medical imaging) is used in Stern-Gerlach-type experiments. However, complementary to these tomographic reconstruction schemes for density matrices relying on Stern-Gerlach-type experiments, our scheme is based on projections of operators onto rotated axial tensor operators or experimentally accessible expectation values of transformed axial tensor operators. The measurement of spherical harmonics components of electromagnetic near-field radiation using specifically designed loop antennas as sensors [57–59] is closely related to our interpretation of droplets as multipole potentials (see Sec. IV).

Further tomographic approaches have been established in [60, 61] with applications to molecular systems. In those works, the quantum state given as the wave functions of an excited state is obtained by decomposing the wave function in a series of basis functions and the expansion coefficients are acquired by calculating a set of Fourier integrals from the detected signal. Also, the wave packet is reconstructed in [62] by computing the overlap

of the state with well-defined reference states for different time intervals.

We want to also contrast our Wigner tomography approach to the so-called spherical tensor analysis (STA) method developed by Suter and Pearson [63] and van Beek et al. [49]. Both Wigner tomography and STA experiments have a similar structure. First, a preparation block (called an excitation sequence in STA) is used to prepare a density operator. In a second step, rotations around several axes are applied in a rotation block. Finally, the density matrix is transformed (by a reconversion sequence in STA) into a detectable basis and the signal is detected during an acquisition period. Despite these similarities and the fact that both methods are based on characteristic properties of spherical tensor operators under rotations, the desired data and therefore also the details of the experiments differ considerably. The goal of STA is not to measure a density operator represented by spherical functions, but to decompose the detectable signal at a later time into individual signal components depending on occurring ranks j and orders m in the current density matrix. In the standard form of STA [49, 63], the detected signal of a density matrix is not characterized or decomposed in terms of additional quantum numbers or labels ℓ . While a single reconversion sequence is used in STA, different pulse sequences are applied in the Wigner tomography in order to transform operators to directly detectable ones (see Fig. 7(c), (d) and Table V). As a final difference, a rotation block in STA uses rotations for three Euler angles α , β , and γ , whereas in the Wigner tomography only two Euler angles α and β are necessary.

Lastly, our Wigner tomography can be seen as a stepping stone along the path to identifying and characterizing operators in terms of expansion coefficients for a suitable chosen basis. One can consider various different bases such as simple matrix coefficients, a spherical tensor basis [30, 63] (as the one used here), or a Cartesian product basis [16, 45, 64–66]. In this context of quantum state tomography, the shapes of spherical functions recovered in the Wigner tomography clearly contain highly redundant information, but they also provide information about random or systematic errors of the tomography process itself. One can also envision Wigner tomography as a component of a more general approach where one would like to optimize the number and location of samples for achieving a desired fidelity and robustness against experimental errors [67, 68], or recover a physical density matrix and estimate experimental errors (see, e.g., [69–75] and references therein).

ACKNOWLEDGMENTS

This work was supported in part by the Excellence Network of Bavaria (ENB) through ExQM. R.Z. and S.J.G. acknowledge support from the Deutsche Forschungsgemeinschaft (DFG) through Grant No. Gl 203/7-2. We

thank Raimund Marx for providing the samples. The experiments were performed at the Bavarian NMR Center at the Technical University of Munich.

Appendix A: Proof of Result 1

We detail now the arguments leading to our reconstruction formula for a spherical function $g(\theta, \phi)$ as stated in Result 1. This result relies on projections of rotated spherical harmonics.

We use the notation introduced in Sec. III. The angles θ and ϕ indicate generic argument values of a spherical function $g(\theta, \phi)$, but the angles β and α refer to specific argument values. First, the right hand side $s_j \langle R_{\alpha\beta} Y_{j0}(\theta, \phi) | g(\theta, \phi) \rangle_{L^2}$ of Eq. (4) in Result 1 is rewritten as $s_j \langle R_{\alpha\beta} Y_{j0}(\theta, \phi) | g_j(\theta, \phi) \rangle_{L^2}$, where the familiar orthogonality relation $\langle Y_{jm}(\theta, \phi) | Y_{j'm'}(\theta, \phi) \rangle_{L^2} = \delta_{jj'} \delta_{mm'}$ of spherical harmonics (see p. 68 of [35]) implies the relation $\langle g_j(\theta, \phi) | g_{j'}(\theta, \phi) \rangle_{L^2} = \delta_{jj'}$ for the rank- j parts $g_j(\theta, \phi)$ in the decomposition $g(\theta, \phi) = \sum_j g_j(\theta, \phi)$. Second, one obtains that $s_j \langle R_{\alpha\beta} Y_{j0}(\theta, \phi) | g_j(\theta, \phi) \rangle_{L^2} = s_j \langle Y_{j0}(\theta, \phi) | R_{\alpha\beta}^{-1} g_j(\theta, \phi) \rangle_{L^2}$ holds, which can be deduced from the invariance $\langle R_{\alpha\beta} Y_{jm}(\theta, \phi) | R_{\alpha\beta} Y_{j'm'}(\theta, \phi) \rangle_{L^2} = \langle Y_{jm}(\theta, \phi) | Y_{j'm'}(\theta, \phi) \rangle_{L^2}$ under rotations. The last relation is easily verified using the formula $R_{\alpha\beta} Y_{jm}(\theta, \phi) = Y_{jm}(\theta - \beta, \phi - \alpha)$ and a change of variables in the integral defining the scalar product (see Sec. III). Finally, $R_{\alpha\beta}^{-1} g_j(\theta, \phi)$ is expanded into a linear combination $\sum_{m'=-j}^j c_{jm'}(\alpha, \beta) Y_{jm'}(\theta, \phi)$ of spherical harmonics [76]. It follows that the right hand side of Eq. (4) is given by $s_j \langle Y_{j0}(\theta, \phi) | \sum_{m'=-j}^j c_{jm'}(\alpha, \beta) Y_{jm'}(\theta, \phi) \rangle_{L^2} = s_j c_{j0}(\alpha, \beta)$.

The left hand side of Eq. (4) is transformed into $g_j(\beta, \alpha) = R_{\alpha\beta}^{-1} g_j(0, 0) = \sum_{m'=-j}^j c_{jm'}(\alpha, \beta) Y_{jm'}(0, 0) = s_j c_{j0}(\alpha, \beta)$, where the formula $Y_{jm'}(0, \phi) = s_j \delta_{m'0}$ (see p. 16 of [77]) has been applied. In summary, we have verified that both sides of Eq. (4) agree, which completes the proof of Result 1.

Appendix B: Proof of Result 2

In this appendix, we demonstrate the tomography formula as given in Result 2 for an operator A by applying the reconstruction formula of Result 1. The proof relies on mapping A to (a set of) spherical functions $f^{(\ell)}(\theta, \phi)$ as detailed in Sec. II.

By substituting $g(\theta, \phi)$ with $f^{(\ell)}(\theta, \phi)$ in Result 1 for each label ℓ separately, one obtains that $f_j^{(\ell)}(\beta, \alpha) = s_j \langle R_{\alpha\beta} Y_{j0}(\theta, \phi) | f^{(\ell)}(\theta, \phi) \rangle_{L^2}$. Note that $\langle A^{(\ell)} | B^{(\ell)} \rangle = \langle f_A^{(\ell)} | f_B^{(\ell)} \rangle_{L^2}$ for the spherical functions $f_A^{(\ell)}$ and $f_B^{(\ell)}$ corresponding to the operators A and B , which can easily be verified by expanding the arguments into tensor operators and spherical harmonics and applying

their orthonormality relations. Moreover, the correspondence between operators and spherical functions is covariant under rotations (see Proposition 1(d) in [30]), i.e., the operator $\mathcal{R}_{\alpha\beta} T_{j0}^{(\ell)}$ is mapped to $R_{\alpha\beta} Y_{j0}(\theta, \phi)$ [78]. The last two statements imply that $f_j^{(\ell)}(\beta, \alpha) = s_j \langle \mathcal{R}_{\alpha\beta} T_{j0}^{(\ell)} | A^{(\ell)} \rangle = s_j \langle \mathcal{R}_{\alpha\beta} T_{j0}^{(\ell)} | A \rangle$, where the last step follows as $\langle A^{(\ell)} | A^{(\ell')} \rangle = 0$ if $\ell \neq \ell'$ (which is a consequence of the orthonormality of the tensor operators $T_{jm}^{(\ell)}$). This completes the proof of Eq. (5) in Results 2, and Eq. (6) is then a direct consequence due to the fact that $\mathcal{R}_{\alpha\beta} T_{j0}^{(\ell)} = [\mathcal{R}_{\alpha\beta} T_{j0}^{(\ell)}]^\dagger$ is Hermitian.

Appendix C: Derivation of Eq. (12)

Here, we derive the formula of Eq. (12) given in Result 3 starting from Result 2. In standard NMR experiments, only the signatures of Cartesian product operators [16] that contain a single transverse Cartesian operator I_{ka} with $a \in \{x, y\}$ (such as I_{ka} , $2I_{ka}I_{lz}$, and $4I_{ka}I_{lz}I_{mz}$) can be measured *directly*, and hence the expectation values of axial operators $T_{j0}^{(\ell)}$ are not *directly* accessible. Nevertheless, these expectation values can be measured *indirectly* since the operators $T_{j0}^{(\ell)} = \sum_n r_j^{(\ell,n)} C_j^{(\ell,n)}$ can always be expressed as real linear combinations of (Hermitian) standard Cartesian product operators $C_j^{(\ell,n)}$ [16]. Thus, the tomography formula of Eq. (12) can be rewritten as $f_j^{(\ell)}(\beta, \alpha) =$

TABLE IV. Sequences to prepare the density matrix ρ from the thermal equilibrium state ρ_{th} , note $I_{abc} := I_{1a}I_{2b}I_{3c}$.

No. of spins	Sequence	ρ
1	$[\frac{\pi}{2}]_y(I_1)$	I_x
	$[\frac{\pi}{2}]_{-x}(I_1)$	I_y
	identity operation (do nothing)	I_z
2	$\mathcal{P}_x^{bil} - [\frac{\pi}{2}]_y(I_2)$	$2I_{1x}I_{2x}$
	$\mathcal{P}_y^{bil} - [\frac{\pi}{2}]_{-x}(I_2)$	$2I_{1y}I_{2y}$
	$\mathcal{P}_x^{bil} - [\frac{\pi}{2}]_{-y}(I_1)$	$2I_{1z}I_{2z}$
	$\mathcal{P}_x^{bil} - [\frac{\pi}{2}]_{-x}(I_2)$	$2I_{1x}I_{2y}$
	$\mathcal{P}_y^{bil} - [\frac{\pi}{2}]_y(I_2)$	$2I_{1y}I_{2x}$
3	$\mathcal{P}_x^{bil} - [\frac{\pi}{2}]_y(I_1) - [\frac{\pi}{2}]_{-y}(I_2)$	$2I_{1z}I_{2x}$
	$\mathcal{P}_x^{tril} - [\frac{\pi}{2}]_y(I_2) - [\frac{\pi}{2}]_y(I_3)$	$4I_{xxx}$
	$\mathcal{P}_x^{tril} - [\frac{\pi}{2}]_{-y}(I_1) - [\frac{\pi}{2}]_{-x}(I_1) - [\frac{\pi}{2}]_{-x}(I_2) - [\frac{\pi}{2}]_{-x}(I_3)$	$4I_{yyy}$
	$\mathcal{P}_x^{tril} - [\frac{\pi}{2}]_{-x}(I_2) - [\frac{\pi}{2}]_{-x}(I_3)$	$4I_{xyy}$
	$\mathcal{P}_x^{tril} - [\frac{\pi}{2}]_{-y}(I_1) - [\frac{\pi}{2}]_{-x}(I_1) - [\frac{\pi}{2}]_y(I_2) - [\frac{\pi}{2}]_{-x}(I_3)$	$4I_{yxy}$
	$\mathcal{P}_x^{tril} - [\frac{\pi}{2}]_{-y}(I_1) - [\frac{\pi}{2}]_{-x}(I_1) - [\frac{\pi}{2}]_{-x}(I_2) - [\frac{\pi}{2}]_y(I_3)$	$4I_{yyx}$
	$\mathcal{P}_x^{tril} - [\frac{\pi}{2}]_y(I_2) - [\frac{\pi}{2}]_{-x}(I_3)$	$4I_{xxy}$
	$\mathcal{P}_x^{tril} - [\frac{\pi}{2}]_{-x}(I_2) - [\frac{\pi}{2}]_y(I_3)$	$4I_{xyx}$
	$\mathcal{P}_x^{tril} - [\frac{\pi}{2}]_{-y}(I_1) - [\frac{\pi}{2}]_{-x}(I_1) - [\frac{\pi}{2}]_y(I_2) - [\frac{\pi}{2}]_y(I_3)$	$4I_{yxx}$
	$\mathcal{P}_x^{tril} - [\frac{\pi}{2}]_{-x}(I_2)$	$4I_{xyx}$

TABLE V. Cartesian product operators $C_j^{(\ell,n)}$ with NMR-measurable operators $M_j^{(\ell,n)}$ used in the experiments, note $I_{abc} := I_{1a}I_{2b}I_{3c}$.

ℓ	j	n	$C_j^{(\ell,n)}$	$M_j^{(\ell,n)}$	ℓ	j	n	$C_j^{(\ell,n)}$	$M_j^{(\ell,n)}$
$\{k\}$	1	1	I_{kz}	I_{kx}	τ_2	2	1	$4I_{xzy}$	$4I_{xzz}$
$\{kl\}$	0, 2	1	$2I_{kx}I_{lx}$	$2I_{kx}I_{lz}$	2		1	$4I_{yzx}$	$4I_{yzz}$
		2	$2I_{ky}I_{ly}$	$2I_{ky}I_{lz}$	3		1	$4I_{zxy}$	$4I_{xzz}$
		3	$2I_{kz}I_{lz}$	$2I_{ky}I_{lx}$	4		1	$4I_{zyx}$	$4I_{xzz}$
	1	1	$2I_{kx}I_{ly}$	$2I_{kx}I_{lx}$	τ_3	1	1	$4I_{xzx}$	$4I_{xzz}$
		2	$2I_{ky}I_{lx}$	$2I_{ky}I_{lz}$	2		1	$4I_{yzy}$	$4I_{yzz}$
τ_1	1, 3	1	$4I_{xzx}$	$4I_{xzz}$	3		1	$4I_{zxx}$	$4I_{xzz}$
		2	$4I_{xzx}$	$4I_{xzz}$	4		1	$4I_{zyy}$	$4I_{xzz}$
		3	$4I_{yyz}$	$4I_{yzz}$	2	1	1	$4I_{xyz}$	$4I_{xzz}$
		4	$4I_{yzy}$	$4I_{yzz}$	2		1	$4I_{xzy}$	$4I_{xzz}$
		5	$4I_{zxx}$	$4I_{xzz}$	3		1	$4I_{yxz}$	$4I_{yzz}$
		6	$4I_{zyy}$	$4I_{xzz}$	4		1	$4I_{yzz}$	$4I_{yzz}$
		7	I_{zzz}	$4I_{xzz}$	5		1	$4I_{zxy}$	$4I_{xzz}$
τ_2	1	1	$4I_{xzx}$	$4I_{xzz}$	6		1	$4I_{zyx}$	$4I_{xzz}$
		2	$4I_{xzx}$	$4I_{xzz}$	τ_4	0	1	$4I_{xyz}$	$4I_{xzz}$
		3	$4I_{yyz}$	$4I_{yzz}$	2		1	$4I_{xzy}$	$4I_{xzz}$
		4	$4I_{yzy}$	$4I_{yzz}$	3		1	$4I_{yxz}$	$4I_{yzz}$
		5	$4I_{zxx}$	$4I_{xzz}$	4		1	$4I_{yzz}$	$4I_{yzz}$
		6	$4I_{zyy}$	$4I_{xzz}$	5		1	$4I_{zxy}$	$4I_{xzz}$
					6		1	$4I_{zyx}$	$4I_{xzz}$

$s_j \sum_n r_j^{(\ell,n)} \langle \mathcal{R}_{\alpha\beta} C_j^{(\ell,n)} \rangle_{\rho}$. One obtains that $f_j^{(\ell)}(\beta, \alpha) = s_j \sum_n r_j^{(\ell,n)} \text{Tr}\{C_j^{(\ell,n)} \tilde{\rho}\}$ where $\tilde{\rho} := \mathfrak{R}_{\alpha\beta}^\dagger \rho \mathfrak{R}_{\alpha\beta}$ by exploiting the action $\mathcal{R}_{\alpha\beta} C_j^{(\ell,n)} = \mathfrak{R}_{\alpha\beta} C_j^{(\ell,n)} \mathfrak{R}_{\alpha\beta}^\dagger$ via the operator $\mathfrak{R}_{\alpha\beta} := \exp(-i\alpha \sum_{k=1}^n I_{kz}) \exp(-i\beta \sum_{k=1}^n I_{ky})$ and the fact that the trace is invariant under cyclic permutations. The operators $C_j^{(\ell,n)}$ can be transformed into measurable operators $M_j^{(\ell,n)} = U_j^{(\ell,n)} C_j^{(\ell,n)} U_j^{(\ell,n)\dagger}$ with unitary transformations $U_j^{(\ell,n)}$, which can be realized experimentally using radio-frequency pulses and coupling evolutions. Hence, the formula of Eq. (12)

is given by $f_j^{(\ell)}(\beta, \alpha) = s_j \sum_n r_j^{(\ell,n)} \text{Tr}\{M_j^{(\ell,n)} \tilde{\rho}^{\ell,j,n}\}$, where immaterial cyclic permutations of the trace have again been applied and where $\tilde{\rho}^{\ell,j,n} := U_j^{(\ell,n)} \tilde{\rho} U_j^{(\ell,n)\dagger}$. Finally, the definition of the expectation value yields $f_j^{(\ell)}(\beta, \alpha) = s_j \sum_n r_j^{(\ell,n)} \langle M_j^{(\ell,n)} \rangle_{\tilde{\rho}^{\ell,j,n}}$.

Appendix D: Preparation and detection sequences

We detail the explicit form of the preparation and detection sequences used in the experiments in order to demonstrate our Wigner tomography. We denote a pulse with flip angle β and phase α that is applied to spin k by $[\beta]_\alpha(I_k)$. Similarly, $[\beta]_\alpha(I_k, I_l)$ specifies two pulses both of flip angle β and phase α that are simultaneously applied to spins k and l . We also use the notation $\mathcal{P}_{x,y}^{bil} = [\frac{\pi}{2}]_y(I_2) - G - [\frac{\pi}{2}]_{x,y}(I_1) - t_a - [\pi]_{y,x}(I_1, I_2) - t_a$ which represents a pulse sequence which is read from left to right. Here, G represents a pulsed magnetic field gradient that dephases all present transverse spin operators and t_a refers to a time delay of length $1/(4J_{12})$, where J_{12} is the coupling constant between the first and second spin. The pulse sequences \mathcal{P}_x^{bil} and \mathcal{P}_y^{bil} create from I_z the bilinear product operators $2I_{1x}I_{2z}$ and $2I_{1y}I_{2z}$, respectively. Moreover, the trilinear product operator $4I_{xzz} := 4I_{1x}I_{2z}I_{3z}$ is obtained from I_z by applying the pulse sequence $\mathcal{P}_x^{tril} = [\frac{\pi}{2}]_y(I_2, I_3) - G - [\frac{\pi}{2}]_y(I_1) - t_b - [\pi]_y(I_1, I_3) - t_c - [\pi]_y(I_2) - t_d$ where the time delays are $t_b = 1/(4J_{13})$, $t_c = 1/(4J_{13}) - 1/(4J_{12})$, and $t_d = 1/(4J_{12})$. Using these notations, the preparation sequences are given in Table IV.

For the detection, the Cartesian product operators $C_j^{(\ell,n)}$ have to be rotated into NMR-measurable operators $M_j^{(\ell,n)}$. The relevant pairs of operators $C_j^{(\ell,n)}$ and $M_j^{(\ell,n)}$ are provided in Table V. The rotation pulse sequences are easily inferred, e.g., one uses the pulse $[\pi/2]_y(I_k)$ in order to rotate I_{kz} into I_{kx} . Similarly, $[\pi/2]_{-y}(I_k)$, $[\pi/2]_x(I_k)$, and $[\pi/2]_{-x}(I_k)$ rotate respectively I_{kx} , I_{ky} , and I_{kz} into I_{kz} , I_{kz} , and I_{ky} . For example, $4I_{zxy}$ is rotated into $4I_{xzz}$ using the pulse sequence $[\frac{\pi}{2}]_x(I_3) - [\frac{\pi}{2}]_{-y}(I_2) - [\frac{\pi}{2}]_y(I_1)$.

- [1] D. T. Smithey, M. Beck, M. G. Raymer, and A. Faridani, Phys. Rev. Lett. **70**, 1244 (1993).
- [2] D. T. Smithey, M. Beck, J. Cooper, M. G. Raymer, and A. Faridani, Phys. Scripta **1993**, 35 (1993).
- [3] D. T. Smithey, M. Beck, J. Cooper, and M. G. Raymer, Phys. Rev. A **48**, 3159 (1993).
- [4] U. Leonhardt, *Measuring the Quantum State of Light* (Cambridge University Press, Cambridge, England, 1997).
- [5] M. Paris and J. Rehacek, eds., *Quantum State Estimation* (Springer, Berlin, 2004).
- [6] E. Wigner, Phys. Rev. **40**, 749 (1932).
- [7] W. P. Schleich, *Quantum Optics in Phase Space* (Wiley-VCH, Weinheim, 2001).
- [8] T. L. Curtright, D. B. Fairlie, and C. K. Zachos, *A Concise Treatise on Quantum Mechanics in Phase Space* (World Scientific, Singapore, 2014).
- [9] H. M. Nussenzveig, *Introduction to Quantum Optics* (Gordon and Breach, New York, 1973).
- [10] W. K. Wootters, Ann. Phys. **176**, 1 (1987).
- [11] U. Leonhardt, Phys. Rev. A **53**, 2998 (1996).
- [12] C. Miquel, J. P. Paz, and M. Saraceno, Phys. Rev. A **65**, 062309 (2002).
- [13] C. Miquel, J. P. Paz, M. Saraceno, E. Knill, R. Laflamme, and C. Negrevergne, Nature **418**, 59 (2002).
- [14] K. S. Gibbons, M. J. Hoffman, and W. K. Wootters, Phys. Rev. A **70**, 062101 (2004).
- [15] C. Ferrie and J. Emerson, New J. Phys. **11**, 063040

- (2009).
- [16] R. R. Ernst, G. Bodenhausen, and A. Wokaun, *Principles of Nuclear Magnetic Resonance in One and Two Dimensions* (Clarendon Press, Oxford, 1987).
- [17] D. G. Donne and D. G. Gorenstein, *Concepts Magn. Reson.* **9**, 95 (1997).
- [18] R. Freeman, *A Handbook of Nuclear Magnetic Resonance*, 2nd ed. (Addison-Wesley, Harlow, 1997).
- [19] R. L. Stratonovich, *J. Exp. Theor. Phys. (USSR)* **31**, 1012 (1956).
- [20] J. C. Várilly and J. M. Garcia-Bondía, *Ann. Phys.* **190**, 107 (1989).
- [21] C. Brif and A. Mann, *Phys. Rev. A* **59**, 971 (1999).
- [22] A. B. Klimov and P. Espinoza, *J. Phys. A* **35**, 8435 (2002).
- [23] A. B. Klimov and P. Espinoza, *J. Opt. B* **7**, 183 (2005).
- [24] C. Brif and A. Mann, *J. Phys. A* **31**, L9 (1997).
- [25] A. Klimov, *J. Math. Phys.* **43**, 2202 (2002).
- [26] J. P. Dowling, G. S. Agarwal, and W. P. Schleich, *Phys. Rev. A* **49**, 4101 (1994).
- [27] P. S. Jessen, D. L. Haycock, G. Klose, G. A. Smith, I. H. Deutsch, and G. K. Brennen, *Quantum Inf. Comput.* **1** (Special Issue), 20 (2001).
- [28] D. J. Philp and P. W. Kuchel, *Concepts Magn. Reson. A* **25A**, 40 (2005).
- [29] D. Harland, M. J. Everitt, K. Nemoto, T. Tilma, and T. P. Spiller, *Phys. Rev. A* **86**, 062117 (2012).
- [30] A. Garon, R. Zeier, and S. J. Glaser, *Phys. Rev. A* **91**, 042122 (2015).
- [31] A. M. Childs, I. L. Chuang, and D. W. Leung, *Phys. Rev. A* **64**, 012314 (2001).
- [32] E. Wigner, *Gruppentheorie und ihre Anwendung auf die Quantenmechanik der Atomspektren* (Friedrich Vieweg & Sohn, Braunschweig, 1931) (English translation in [33]).
- [33] E. P. Wigner, *Group Theory and its Application to the Quantum Mechanics of Atomic Spectra* (Academic Press, London, 1959).
- [34] G. Racah, *Phys. Rev.* **62**, 438 (1942).
- [35] L. C. Biedenharn and J. D. Louck, *Angular Momentum in Quantum Physics* (Addison-Wesley, Reading, MA, 1981).
- [36] B. L. Silver, *Irreducible Tensor Methods* (Academic Press, New York, 1976).
- [37] M. Chaichian and R. Hagedorn, *Symmetries in Quantum Mechanics: From Angular Momentum to Supersymmetry* (Institute of Physics, Bristol, 1998).
- [38] J. D. Jackson, *Classical Electrodynamics*, 3rd ed. (Wiley, New York, 1999).
- [39] Spherical harmonics $Y_{jm}(\theta, \phi) = r(\theta, \phi) \exp[i\eta(\theta, \phi)]$ (and spherical functions) are plotted throughout this paper by mapping their spherical coordinates θ and ϕ to the radial part $r(\theta, \phi)$ and phase $\eta(\theta, \phi)$.
- [40] N. J. Glaser and S. J. Glaser, “SpinDrops [Mobile application],” (2014), itunes.apple.com.
- [41] Cartesian operators for single spins are $I_x := \sigma_x/2$, $I_y := \sigma_y/2$, and $I_z := \sigma_z/2$, where the Pauli matrices are $\sigma_x = \begin{pmatrix} 0 & 1 \\ 1 & 0 \end{pmatrix}$, $\sigma_y = \begin{pmatrix} 0 & -i \\ i & 0 \end{pmatrix}$, and $\sigma_z = \begin{pmatrix} 1 & 0 \\ 0 & -1 \end{pmatrix}$. For n spins, one has the operators $I_{k\eta} := \bigotimes_{s=1}^n I_{a_s}$ where a_s is equal to η for $s=k$ and is zero otherwise; note $I_0 := \begin{pmatrix} 1 & 0 \\ 0 & 1 \end{pmatrix}$.
- [42] Hermitian operators lead to positive and negative values which are shown in red (dark gray) and green (light gray).
- [43] B. E. Sagan, *The Symmetric Group*, 2nd ed. (Springer, New York, 2001).
- [44] M. A. Nielsen and I. L. Chuang, *Quantum Computation and Quantum Information* (Cambridge University Press, Cambridge, England, 2000).
- [45] I. L. Chuang, N. Gershenfeld, and M. Kubinec, *Phys. Rev. Lett.* **80**, 3408 (1998).
- [46] M. H. Levitt, *Spin Dynamics: Basics of Nuclear Magnetic Resonance* (Wiley, New York, 2008).
- [47] A. Tabuchi, M. Negoro, K. Takeda, and M. Kitagawa, *J. Magn. Reson.* **204**, 327 (2010).
- [48] M. P. Augustine and E. L. Hahn, *Concepts Magn. Reson.* **13**, 1 (2001).
- [49] J. D. van Beek, M. Carravetta, G. C. Antonioli, and M. H. Levitt, *J. Chem. Phys.* **122**, 244510 (2005).
- [50] V. I. Lebedev, *USSR Comput. Math. Math. Phys.* **15**, 44 (1975).
- [51] V. I. Lebedev, *USSR Comput. Math. Math. Phys.* **16**, 10 (1976).
- [52] V. I. Lebedev and D. N. Laikov, *Russian Acad. Sci. Dokl. Math.* **59**, 477 (1999).
- [53] B. Koczor, R. Zeier, and S. J. Glaser, arXiv:1612.06777.
- [54] T. Tilma, M. J. Everitt, J. H. Samson, W. J. Munro, and K. Nemoto, *Phys. Rev. Lett.* **117**, 180401 (2016).
- [55] R. P. Rundle, P. W. Mills, T. Tilma, J. H. Samson, and M. J. Everitt, *Phys. Rev. A* **96**, 022117 (2017).
- [56] R. Schmied and P. Treutlein, *New J. Phys.* **13**, 065019 (2011).
- [57] B. Vincent, O. Chadebec, J.-L. Schanen, C. A. F. Sartori, L. Krähenbühl, R. Perrussel, and K. Berger, *J. Microw. Optoelectron. Electromagn. Appl.* **8**, 64S (2009).
- [58] B. Vincent, O. Chadebec, J. L. Schanen, and K. Berger, *IEEE Trans. Instrum. Meas.* **59**, 3086 (2010).
- [59] A. Bréard, F. Tavernier, Z. Li, and L. Krähenbühl, *IEEE Trans. Magn.* **52**, 1 (2016).
- [60] D. Avisar and D. J. Tannor, *Phys. Rev. Lett.* **106**, 170405 (2011).
- [61] C. Menzel-Jones and M. Shapiro, *J. Phys. Chem. Lett.* **3**, 3353 (2012).
- [62] T. S. Humble and J. A. Cina, *Phys. Rev. Lett.* **93**, 060402 (2004).
- [63] D. Suter and J. Pearson, *Chem. Phys. Lett.* **144**, 328 (1988).
- [64] I. L. Chuang, N. Gershenfeld, M. G. Kubinec, and D. W. Leung, *Proc. R. Soc. A* **454**, 447 (1998).
- [65] R. Das, T. S. Mahesh, and A. Kumar, *Phys. Rev. A* **67**, 062304 (2003).
- [66] G. M. Leskowitz and L. J. Mueller, *Phys. Rev. A* **69**, 052302 (2004).
- [67] A. Miranowicz, K. Bartkiewicz, J. Peřina, M. Koashi, N. Imoto, and F. Nori, *Phys. Rev. A* **90**, 062123 (2014).
- [68] L. L. Rouve, L. Schmerber, O. Chadebec, and A. Foggia, *IEEE Trans. Magn.* **42**, 1167 (2006).
- [69] C. Schwemmer, L. Knips, D. Richart, H. Weinfurter, T. Moroder, M. Kleinmann, and O. Gühne, *Phys. Rev. Lett.* **114**, 080403 (2015).
- [70] L. Knips, C. Schwemmer, N. Klein, J. Reuter, G. Tóth, and H. Weinfurter, arXiv:1512.06866.
- [71] P. Faist and R. Renner, *Phys. Rev. Lett.* **117**, 010404 (2016).
- [72] G. B. Silva, S. Glancy, and H. M. Vasconcelos, *Phys. Rev. A* **95**, 022107 (2017).
- [73] A. Steffens, C. A. Riofrí, W. McCutcheon, I. Roth, B. A. Bell, A. McMillan, M. S. Tame, J. G. Rarity, and J. Eisert, *Quantum Sci. Technol.* **2**, 025005 (2017).
- [74] C. A. Riofrí, D. Gross, S. T. Flammia, T. Monz, D. Nigg, R. Blatt, and J. Eisert, *Nat. Commun.* **8**, 15305 (2017).
- [75] D. Suess, L. Rudnicki, T. O. Maciel, and D. Gross, *New*

J. Phys **19**, 093013 (2017).

- [76] Even though our arguments do not rely on explicitly knowing the expansion coefficients $c_{jm'}(\alpha, \beta)$, it might be instructive to specify the expansion coefficients in terms of the widely used Wigner- D matrices $D_{m'm}^j(\alpha, \beta, \gamma)$ [35, 77]. Let us also assume that the rank- j parts $g_j(\theta, \phi)$ are expanded into $g_j(\theta, \phi) = \sum_{m=-j}^j \tilde{c}_{jm} Y_{jm}(\theta, \phi)$ using certain coefficients \tilde{c}_{jm} . The theory of Wigner- D matrices [35, 77] implies that $R_{\alpha\beta}^{-1} Y_{jm}(\theta, \phi) = \sum_{m'=-j}^j D_{m'm}^j(0, -\beta, -\alpha) Y_{jm'}(\theta, \phi)$. Hence, we obtain the formula $R_{\alpha\beta}^{-1} g_j(\theta, \phi) = \sum_{m=-j}^j$

$\tilde{c}_{jm} \times \sum_{m'=-j}^j D_{m'm}^j(0, -\beta, -\alpha) Y_{jm'}(\theta, \phi)$ which shows that $c_{jm'}(\alpha, \beta) = \sum_{m=-j}^j \tilde{c}_{jm} D_{m'm}^j(0, -\beta, -\alpha)$.

- [77] E. O. Steinborn and K. Rueddenberg, Adv. Quantum Chem. **7**, 1 (1973).
- [78] This relation can also be established using the theory of Wigner- D matrices [35, 77] where $D_{m'm}^j(\alpha, \beta, \gamma) = \langle Y_{jm'}(\theta, \phi) | R_{\alpha\beta\gamma} Y_{jm}(\theta, \phi) \rangle_{L^2}$ (see p. 41 and 276 of [35]) and $D_{m'm}^j(\alpha, \beta, \gamma) = \langle T_{jm'}^{(\ell)} | \mathcal{R}_{\alpha\beta\gamma} T_{jm}^{(\ell)} \rangle$ (see p. 45 of [35]). Here, $\mathcal{R}_{\alpha\beta\gamma} C := \mathfrak{R}_{\alpha\beta\gamma} C \mathfrak{R}_{\alpha\beta\gamma}^{-1}$ with $\mathfrak{R}_{\alpha\beta\gamma} := e^{-i\alpha F_z} e^{-i\beta F_y} e^{-i\gamma F_z}$ (see Sec. III) where $\mathcal{R}_{\alpha\beta} = \mathcal{R}_{\alpha\beta 0}$.